Indian Journal of Chemical Technology
Vol. 29, November 2022, pp. 688-696
DOI: 10.56042/ijct.v29i6.67363

Comparative analysis on electrochemical properties of CeO_2/rGO and CeO_2/MoS_2 nanocomposites for supercapacitor applications

Mohamed Ismail M[1,2], Aishwarya J[2], Prasath J[1], Alagar Nedunchezhian A S[1], Manimuthu V[3], Arivanandhan M*[,1,4],
Sivakumar T[2,4], I Sarris[5] & Jayavel R[1,4]

[1]Center for Nanoscience and Technology, Anna University, Chennai 600 025, India
[2]Department of Applied Science and Technology, Anna University, Chennai 600 025, India
[3]Department of Material Science, University of Madras, Chennai 600 005, India
[4]Centre for Energy Storage Technologies, Anna University, Guindy, Chennai 600 025, India
[5]Department of Mechanical Engineering, University of West Attica, Athens, Greece
E-mail: arivucz@gmail.com

Received 19 August 2022; accepted 21 October 2022

The supercapacitor is an intriguing future energy storage device. 2D nanomaterials such as Graphene oxide (GO) and MoS_2 are well-known electrostatic double layer capacitance (EDLC) based electrode materials. In the present work, the effect of compositing CeO_2 with GO and MoS_2 on their electrochemical performance has been investigated. The crystal structure of the pure CeO_2 and composites were confirmed by XRD analysis. Raman spectroscopic analysis revealed the F_{2g} vibration mode of CeO_2, D and G bands of GO nanosheets. SEM analysis confirmed the spherical morphology of CeO_2 nanoparticle and sheets like morphology of rGO and MoS_2. The SEM images of composites show the presence of spherical particles and nanosheets, which confirm the formation of CeO_2/rGO and CeO_2/MoS_2 nanocomposites. The electrochemical characteristics of CeO_2/rGO and CeO_2/MoS_2 nanocomposites-based electrode materials were evaluated using cyclic voltammetry (CV), chronopotentiometry (CP), and EIS analyses. The CeO_2, CeO_2/MoS_2, and CeO_2/rGO electrodes exhibited the specific capacitance of 660, 866, and 959 Fg^{-1}, respectively at $5mVs^{-1}$. Due to the synergistic effect of CeO_2 with rGO and MoS_2, the CeO_2/rGO and CeO_2/MoS_2 nanocomposite electrode materials have shown improved energy storage performance compared to pure CeO_2.

Keywords: CeO_2, rGO, MoS_2, Nanocomposite, Raman spectroscopy, Supercapacitor, XRD

In response to ever-increasing energy consumption and technological advancements, the scientific community has made energy storage a primary focus area of research[1-3]. Supercapacitors have received great research interest for energy storage applications. In particular, to develop a Li-ion battery along with supercapacitor as a hybrid energy storage device in electric vehicles, electronic gadgets, and grids, significant attention must be given to the energy density, power density, internal resistance, and cycle stability of the supercapacitor[4-6]. To construct supercapacitors with desired energy density, suitable electrode materials with high electrical conductivity, high surface area, high thermal and chemical stability, and good electrochemical reversibility are essential. The electrode material mostly determines the performance of a supercapacitor. In recent times, research has been focused on a diversity of electrode materials, including high surface area carbonaceous materials, metal oxide/sulfide/nitride, conducting polymers and nanocomposites[7].

Generally, carbon-based electrode materials have shown high power density and long cycle life, but they exhibited a low specific capacitance value that limits their applications[8]. Alternatively, Transition metal oxides (TMOs) such as RuO_2, NiO, Co_3O_4 and MnO_2 have been previously reported as supercapacitor electrodes due to their high theoretical specific capacitance and fast reversible redox reactions[9-12]. However, the TMOs have some problems, such as high cost, low conductivity, and poor stability. To overcome these problems, environmental friendly, cost-effective, and high-performance materials can be used as an electrode.

Cerium Oxide (CeO_2) is one of the rare earth (RE) metal oxides with pseudocapacitance behaviour. Despite being a RE element, cerium is quite common in the earth's crust. It is the most ubiquitous of the Lanthanides. It is one of the 78 common elements in the earth's crust, ranking 25th in prevalence with a 20–60 ppm average distribution. It has a unique structure and peculiar redox and catalytic properties due to their oxygen storage capacity[13]. It has two oxidation states, 3^+ and 4^+. The variation in oxidation state is beneficial for redox reactions in electrochemical energy storage process. Moreover, nano CeO_2 provides maximal reactivity and thermodynamic stability.[14] It is inferred that the graphene oxide-based CeO_2 nanocomposite exhibits high specific capacitance due to the combination of EDLC and pseudocapacitance behaviour[15-21]. MoS_2 is a semiconducting 2D material. The combination of CeO_2/MoS_2 increases specific capacitance over pure CeO_2. However, the electrochemical properties of CeO_2/MoS_2 nanocomposites have been rarely investigated. The presence of GO and MoS_2 inhibits aggregation, facilitates the electrolyte ions' interface with the electrode, and restricts the structural changes of CeO_2 nanoparticles[22-31]. Moreover, the electrochemical properties of CeO_2/rGO and CeO_2/MoS_2 nanocomposites need to be investigated further to improve their performance. Therefore, the purpose of the present work is to synthesize CeO_2, CeO_2/rGO, and CeO_2/MoS_2 nanocomposites and comparatively investigate their structural, morphological, and electrochemical properties. The electrochemical performance of pure CeO_2, CeO_2/rGO, and CeO_2/MoS_2 composite materials were examined using cyclic voltammetry (CV), chronopotentiometry (CP) and Electrochemical Impedance Spectroscopy (EIS).

Experimental Section

Synthesis of cerium oxide nanoparticles

The microwave-assisted method was used to synthesis CeO_2. Hydrated cerium nitrate (Alfa aesar, 99.5%) was used as a precursor to synthesis cerium oxide. Initially, 0.1 M of cerium nitrate was mixed with 0.2 M of citric acid in 30 mL of ethylene glycol solvent at 100°C, under stirring condition. It must be ensured that the solution was completely transparent. The solution was placed in the microwave oven (850 watts) for 1 min. The solution was transformed into yellow colour. Following that, ammonium hydroxide (NH_4OH) was added to the obtained solution and system was brought to a higher *p*H value under the stirring for 30 min. Simultaneously, water was gradually added to the solution until a volume of 220 ml was obtained. The solution was washed three times with double distilled (DD) water. The CeO_2 powder was obtained by drying the slurry at 100°C in hot air oven for 12 h to give a pale yellow powder.

Synthesis of GO nanosheets

A modified Hummer's method was used to synthesize graphene oxide from graphite powder[32]. To prepare a suspension, graphite powder (3 g) was added to 69 mL of concentrated H_2SO_4 solution and stirred for 45 min in an ice bath. After that, 1.5g of $NaNO_3$ was gradually added and stirred for 30 min. Then, for 3 h, 3g of $KMnO_4$ was slowly added while stirring, and the temperature of the mixture was maintained below 20°C using an ice bath. After that, the temperature was raised to 35°C and the mixture was stirred for 6 hours. The suspension was then diluted in the ice bath with 138 mL of distilled water to keep the temperature below 60°C. After 6 h, 3 mL of H_2O_2 and 300 mL of distilled water were added, and the colour of the suspension changed from dark brown to a turbid yellow solution. To remove the acid, the suspension was washed three times with distilled water and centrifuged at 6000 rpm for 15 min. The GO powder was obtained by drying the dispersion for 24 h at 80°C in a hot air oven.

Synthesis of MoS_2 nanosheets

The hydrothermal method was used to synthesize the MoS_2 nanosheets. In 80 mL of distilled water, 1:3 molar ratio of sodium molybdate ($Na_2MoO_4.2H_2O$) and thioacetamide (C_2H_5NS) were dissolved with constant stirring for half an hour. The solution was then transferred to a Teflon lined stainless steel autoclave and maintained at 180°C in a box furnace for 24 h. The reacted precipitate was then collected and centrifuged three times with distilled water. Finally, the sample was dried at 80°C in a vacuum oven for 12 h.

Synthesis of CeO_2/MoS_2 &CeO_2/GO nanocomposites

The CeO_2/MoS_2 nanocomposite was synthesized by the ultra-sonication method. For synthesizing the composite, 5wt % of MoS_2 was added into the solution dispersed with 300 mg of cerium oxide under continuous stirring at room temperature. Then the sonicated sample was dried at 100°C. A CeO_2/MoS_2 nanocomposite was obtained.

The CeO_2/rGO nanocomposite was synthesized by the ultra-sonication method. To prepare the composite, 15 mg (5wt%) of GO was dispersed in 30 mL of DD water and sonicated for 2 h, followed by the addition of 300 mg of as synthesized CeO_2 powder in the GO dispersed DD water for 1 hour. Then the sonicated sample was dried at 100°C in hot air oven. A CeO_2/rGO nanocomposite was obtained.

Results and Discussion

The XRD analysis was carried out to study the crystal structure and to estimate the crystallite size of the samples. Fig 1 (a-c) shows the XRD patterns of CeO_2/MoS_2, CeO_2/rGO and $\mathbf{CeO_2}$ nanoparticles. The sharp and high intense peaks of CeO_2 illustrate high crystalline nature of the sample. The diffraction pattern of pure CeO_2 contains four major peaks corresponding to (111), (200), (220) and (311) diffraction planes at two theta values of 28.39, 33.34, 47.26, and 55.97 degrees, respectively. The diffraction pattern is well matched with the standard JCPDS no.81-0792, which confirms the cubic fluorite structure of the sample. The full width half maximum of the diffraction peaks of nanocomposites increased compared to pure $\mathbf{CeO_2}$ due to the anchoring of $\mathbf{CeO_2}$ nanoparticles on the 2D materials.

Moreover, rGO and MoS_2 related peaks were not observed in the XRD patterns Fig. 1(a) and (b) of nanocomposite due to least amount of (5%) 2D samples added into the composite. Fig 1(d) and (e) shows the XRD patterns of 2D materials of MoS_2 and rGO, respectively, MoS_2 XRD patterns confirms the formation of 2H hexagonal MoS_2 structure and the pattern is well matched with standard JCPDS card 37-1492. The XRD of rGO sample shows a broad peak at 21 degree which confirms the formation of exfoliated rGO sheet like structures. Both patterns were well broadened and less intense which confirms the formation of 2D materials with sheet like morphology. Furthermore, the calculated crystallite size of the pure CeO_2, CeO_2/rGO and CeO_2/MoS_2 nanocomposites are 9.56, 3.62, and 3.21 nm, respectively, from Debye Scherrer equation (1).

$$D = \frac{K\lambda}{\beta_{\mathrm{hkl}} \cos\theta} \qquad \ldots (1)$$

where D is the crystallite size of the nanoparticle, K the form factor (0.9), λ is the X-ray wavelength, and θ is the X-ray diffraction angle. β is the full width half maximum (FWHM) of the diffraction peak in radians.

The crystallite size of the composites was relatively lesser than the pure CeO_2 nanoparticles. Because, the high surface area 2D materials (rGO and MoS_2) facilitate to anchor the CeO_2 nanoparticles on their surface and well prevent the agglomeration of nanoparticles with well dispersion of CeO_2 nanoparticles.

Raman spectroscopic analysis of $\mathbf{CeO_2}$, and $\mathbf{CeO_2}$ /GO nanocomposites

The Raman analysis revealed the molecular vibrations in cerium oxide and its composites. Figure 2(a) and (b) show the Raman spectra with active vibration modes of CeO_2/MoS_2 nanocomposite and pristine CeO_2 nanoparticles, respectively. The

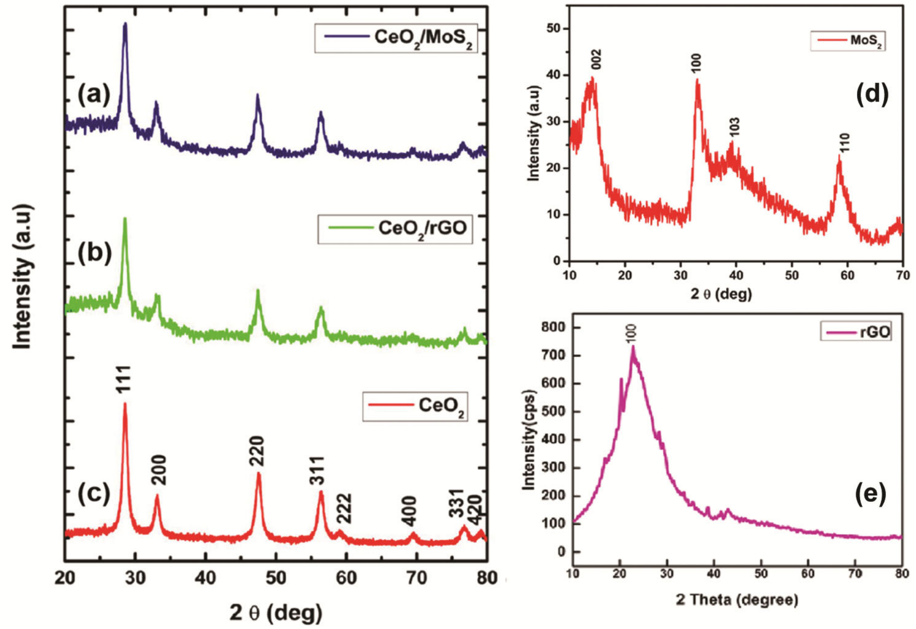

Fig. 1 — XRD patterns of (a) CeO_2/MoS_2 (5 wt%); (b) CeO_2/rGO (5 wt%); (c) CeO_2 nanoparticle; (d) MoS_2 nanosheets and (e) rGO nanosheets.

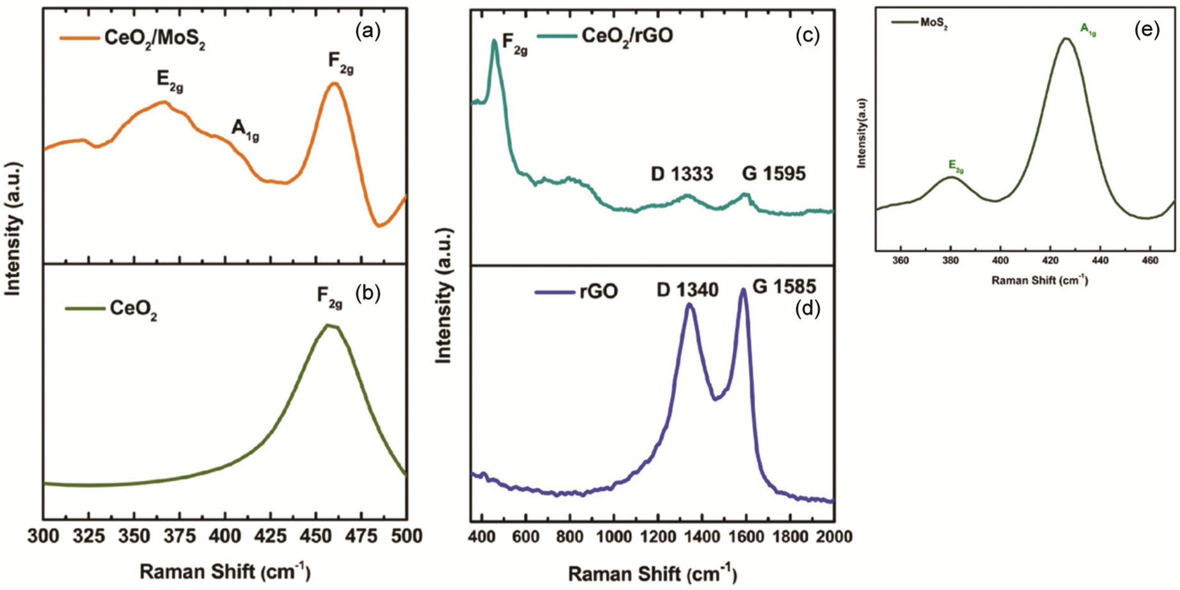

Fig. 2 — Raman spectra of (a) CeO_2/MoS_2 (5 wt%) nanosheets; (b) CeO_2 nanoparticles; (c) CeO_2/rGO (5 wt%) nanosheets; (d) rGO nanosheets and (e) MoS_2 nanosheets

CeO_2 nanoparticles sample shows the vibration peak at 458 cm^{-1} [Fig. 2(b)] which confirms the cubic structure of CeO_2 corresponds to F_{2g} symmetry, and it can be viewed as a symmetric breathing mode of oxygen atoms around each cerium cation. As only the oxygen atoms move, the vibration mode is nearly independent of cation mass. On the other hand, Figure 2(a) shows the Raman spectrum of CeO_2/MoS_2 composite with F_{2g} mode of CeO_2 vibration along with the E_{2g} and A_{1g} modes of vibrations of MoS_2 nanosheets, which confirms the formation of composite. The intensity of MoS_2 related peaks are very weak due to the lower weight percentage of MoS_2 in the composite. Figure 2(c) and (d) depict the Raman spectra of CeO_2/rGO and rGO, respectively. The Raman spectrum of CeO_2/rGO nanocomposite [Fig. 2(c)] consists of the F_{2g} mode of CeO_2 vibration at 461 cm^{-1} with in-plane C-C vibration (G band) of GO at 1595 cm^{-1} and the disorder (D band) of rGO at 1333 cm^{-1} as can be seen in Fig. 2(c). Figure 2(d) shows the Raman spectrum of rGO which exhibits D and G bands at 1340 and 1585 cm^{-1}, respectively. The presence of F_{2g}, D and G bands vibrations in the CeO_2/rGO nanocomposite with a measured intensity ratio of D and G bands (I_D/I_G = 0.83) and peak shift confirms the formation of the CeO_2/rGO nanocomposite. Figure 2 (e) depicts the Raman spectrum of nanostructured MoS_2, which reveals two primary Raman-active modes of E_{2g} and A_{1g}. The E_{2g} mode is an in-plane vibration present at 382 cm^{-1}, while the A_{1g} mode is an out-of-plane lattice expansion at 423 cm^{-1} which confirms the formation of 2D layered MoS_2 nanosheets. These two peaks are clearly observed in the CeO_2/MoS_2 composite which confirms the formation of composite.

FTIR analysis of CeO2, CeO2/rGO & CeO2/MoS2 nanocomposites

Figure 3 shows the FTIR spectra of CeO_2, CeO_2/rGO and CeO_2/MoS_2 nanocomposites. Figure 3(a) depicts the FTIR spectrum of pristine CeO_2 with lower wave number vibration at 458 cm^{-1} confirms the presence of Ce-O stretching of CeO_2 nanoparticles. In addition, hydroxyl group related peaks were observed in the sample due to low temperature processing. Figure 3(b) represents the FTIR spectrum of CeO_2/rGO nanocomposite with various functional groups related peaks of the sample. The vibrational peaks of major functional groups such as C=C, C=O, and OH of rGO were observed at 1551, 1739, and 3342 cm^{-1}, respectively along with CeO_2 vibration a t488 cm^{-1}. Figure 3(c) shows the FTIR spectrum of CeO_2/MoS_2 nanocomposite. The thiol functional group and sulfur functional groups of MoS_2 were observed at 1219 and 1361 cm^{-1} along with CeO_2 vibration peak at lower wave number confirms the formation of CeO_2/MoS_2 nanocomposite.

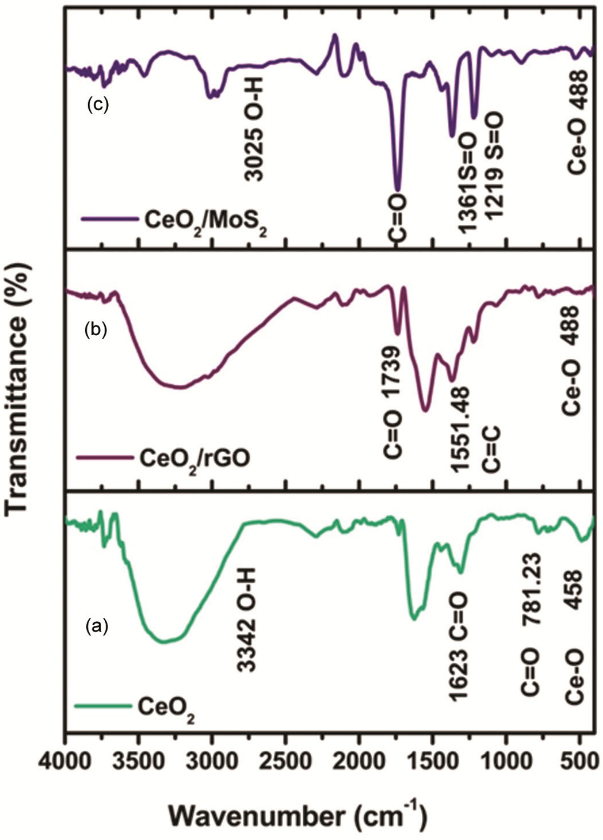

Fig. 3 — FTIR spectra of (a) CeO_2 nanoparticles, (b) rGO nanosheets (c) CeO_2/rGO (5 wt%) nanosheets.

Morphological analysis of CeO_2, CeO_2/rGO& CeO_2/MoS_2 nanocomposites

Figure 4 (a) show the SEM image of cerium oxide, which shows the evenly distributed particles with spherical morphology and the size of the particles is less than 150 nm. Figure 4(b) shows the sheet-like morphology of GO. Figure 4 (c) depict the morphology of CeO_2/rGO nanocomposite, with CeO_2 nanoparticles decorated on the surface of rGO sheets with less agglomeration of nanoparticles. Moreover, size of the CeO_2 nanoparticles is relatively decreased compared to pure sample due to anchoring on rGO sheets. As like GO, the MoS_2 exhibitsthe sheet like morphology depicted in Fig 4 (d). Figure 4 (e) and (f) shows the SEM images of CeO_2/MoS_2 nanocomposite which shows that the CeO_2 nanoparticles decorated on the surface of MoS_2 nanosheets. The CeO_2 nanoparticles were anchored on the MoS_2 nanosheets and thereby the size of the particles. The distribution of nanoparticles in the high surface area 2D materials prevents the agglomeration of nanoparticles, provide structural stability, and improve the ionic and electronic conduction from electrode material to current collector.

Electrochemical studies

Electrode preparation

The electrochemical properties of CeO_2, CeO_2/MoS_2, and CeO_2/rGO electrode materials were studied using CV, CP, and EIS analysis. The working electrode was prepared by mixing 10 mg of electro-active materials of CeO_2, CeO_2/MoS_2, and CeO_2/rGO dispersed in 0.5 mL of ethanol and 20 µL Nafion. The mixture was ultrasonicated for 10 min. Finally, the obtained slurry was coated onto the classy carbon electrode and dried in air. As prepared, CeO_2, CeO_2/MoS_2, CeO_2/rGO as the working electrode, Pt wire and the Ag/AgCl were used as a counter and reference electrodes, respectively. Aqueous 2 M KOH solution serves as the supporting electrolyte. CVs were measured in an electrochemical system for different sweeping rates from 5 to 100 mVs^{-1}. CPs of the electrodes were measured in the potential range of –0.6 to 0.4 V (verses. Ag/AgCl) at different current densities using a electrochemical workstation.

Cyclic voltammetry analysis of CeO_2, CeO_2/rGO, and CeO_2/MoS_2 nanocomposites

The shape of the CV curves in Fig. 5(a) indicates the pseudocapacitive behaviour of the material. The voltammetery current is always directly proportional to the scan rate because, at low scan rate the K^+ ions have more time to intercalate at many active site of electrode material, on the other hand at higher scan rate the K^+ ions were less intercalated due to shorter time for adsorption. As can be seen from Figs 5(b) and (c), the current density of CeO_2/rGO two-fold increased than the CeO_2. The current density of CeO_2/MoS_2 nanocomposite also relatively increased than the pristine CeO_2. The drastic increase in the current density of CeO_2/rGO nanocomposite was due to the high conductive nature of rGO than MoS_2 nanosheets and pristine CeO_2[25-28]. The maximum specific capacitance of 660 Fg^{-1} was obtained for CeO_2 at a lower scan rate at 10 mVs^{-1}.

Figure 5(d) shows the comparison of CV curves of CeO_2, CeO_2/MoS_2 and CeO_2/rGO. The area of CV curve was increased for CeO_2/rGO nanocomposite compared to other samples. Hence, CeO_2/rGO shows the high Specific Capacitance of 959 Fg^{-1} whereas CeO_2/MoS_2 shows 866 Fg^{-1} at 10 mVs^{-1}. rGO has high surface area compared to MoS_2 thereby the adsorption and storage capacity of rGO based nanocomposite was relatively higher than other samples. Table 1 shows the calculated specific capacitance values of CeO_2, CeO_2/MoS_2, CeO_2/rGO electrodes from CV.

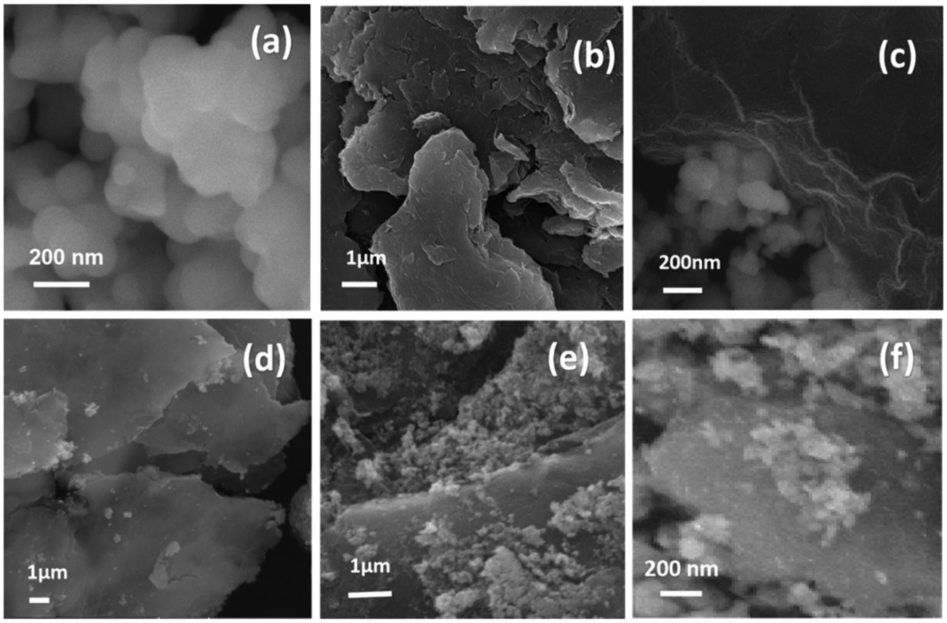

Fig. 4 — SEM images of (a) CeO_2 nanoparticles; (b) GO; (c) CeO_2/rGO (5 wt%) nanocomposite; (d) MoS_2 nanosheets and (e & f) CeO_2/MoS_2 (5 wt%) nanocomposite.

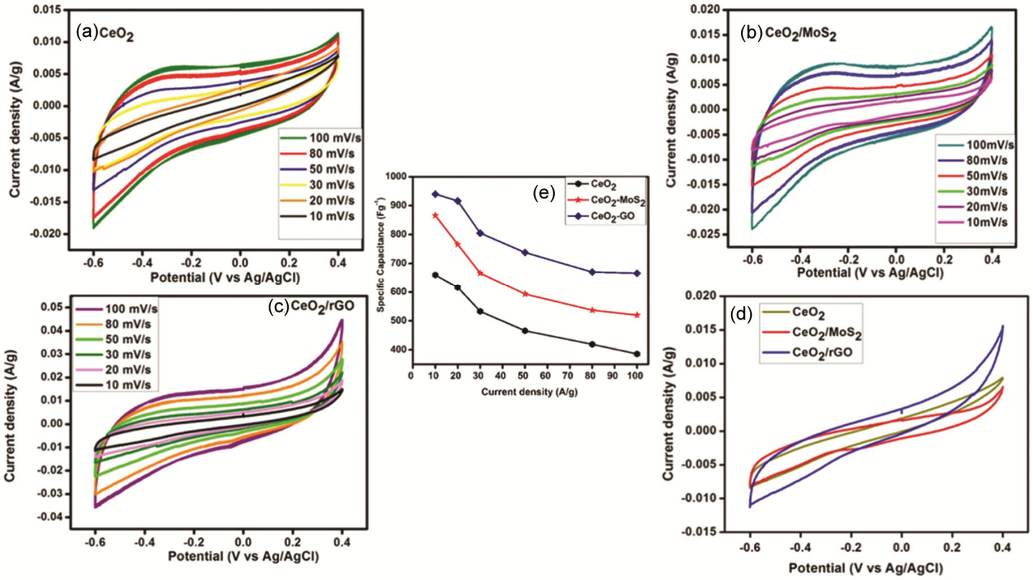

Fig. 5 — CV curves of (a) CeO_2; (b) CeO_2/MoS_2; (c) CeO_2/rGO; (d) comparison of CV curves of CeO_2, CeO_2/MoS_2 & CeO_2/rGO at 10 mVs^{-1} and (e) specific capacitance of CeO_2, CeO_2/MoS_2 & CeO_2/rGO

Figure 5(e) shows the variation of specific capacitance with scan rate for various electrodes. The specific capacitance of all electrodes decreases with the increasing scan rate from 10 to 100 mVs^{-1}, due to the reduced intercalation of electrolyte into the pores of electrode materials[33,34].

The CP charge/discharge profiles of CeO_2, CeO_2/rGO and CeO_2/MoS_2 are shown in Fig 6 (a-d). Figure 6 (a) shows the CP curves of CeO_2 nanoparticles recorded at various current densities from 0.06 to 1 Ag^{-1}.The curves are symmetric and charge and discharge time increased with decreasing current densities. At higher current density the electrolyte ions adsorbed at limited active sites on surface of the electrode materials, which reduce surface redox reactions at electrode/electrolyte

Table 1 — Specific capacitance values of CeO_2, CeO_2/MoS_2, and CeO2/rGO from CV curve.

Scan rate (mVs^{-1})	Specific capacitance of CeO_2 (Fg^{-1})	Specific capacitance of CeO_2/MoS_2(Fg^{-1})	Specific capacitance of CeO_2/rGO (Fg^{-1})
10	660	866	959
20	616	766	927
30	533	666	820
50	466	593	750
80	419	537	727
100	386	520	697

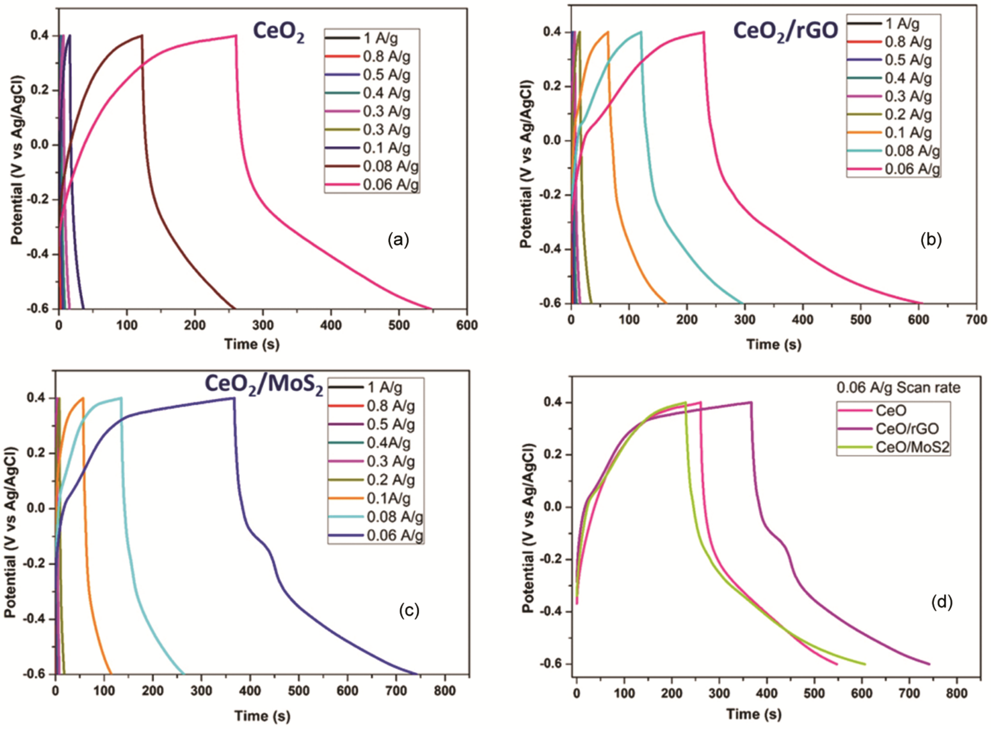

Fig. 6 — Charge and discharge curve of (a) CeO_2 nanoparticles; (b) CeO_2/rGO (5 wt. %); (c) CeO_2/MoS_2 (5 wt. %) and (d) comparative CP curve of electrodes at 0.06 Ag^{-1}

interface. Whereas at lower current densities the electrolyte ions adsorbed at almost all the active sites on the surface area of the electrode material which increase the surface redox reaction at electrode/electrolyte interface. Hence the sample exhibit prolonged discharge time for lower current densities. The CeO_2/rGO electrode shows prolonged discharge time compared to other electrodes. From the discharge curve, the specific capacitance was calculated for CeO_2, CeO_2/rGO, and CeO_2/MoS_2. The composite electrodes shown the maximum specific capacitance (CeO_2/rGO - 911 Fg^{-1}) (CeO_2/MoS_2 -877 Fg^{-1}) compared to pristine CeO_2 (128 Fg^{-1}) electrode at a constant current density of 0.3 Ag^{-1}. The symmetric charge discharge curve shows the profound capacitive nature of the electrode material[16-20]. The calculated specific capacitance of the prepared pure and composite electrodes is compared with reported values of similar electrode materials in Table 2.

EIS analysis of CeO_2, CeO_2/rGO, and CeO_2/MoS_2 nanocomposites

Electrochemical charge storage performance of CeO_2, CeO_2/rGO, and CeO_2/MoS_2 electrodes was further analysed through EIS studies. The semicircle region in Fig. 7 shows the Faradaic charge transfer process of CeO_2 material, which confirms the pseudocapacitive behaviour of the material. The equivalence series resistance (R_{ESR}) of the CeO_2 was 0.5 Ωwhich is relatively lower than CeO_2/rGO (2.3 Ω), and CeO_2/MoS_2 (2.7 Ω) respectively. Moreover, the semicircle region was decreased in

Table 2 — Comparison of capacitance values for various CeO_2-based electrodes

Electrode materials	Electrolyte	Specific capacitance (Fg^{-1})	Ref. No
CeO_2/rGO	0.5 M Na_2SO_4	211	12
CeO_2/N-rGO	6 M KOH	230	13
CeO_2/CNT	0.5 M Na_2SO_4	289	14
Co_3O_4-CeO_2	3 M KOH	1288	17
CeO_2/C	3 M KOH	602	16
rGO/CeO_2	3 M KOH	265	15
CeO_2	2 M KOH	660	Present work
CeO_2/MoS_2		866	
CeO_2/rGO		959	

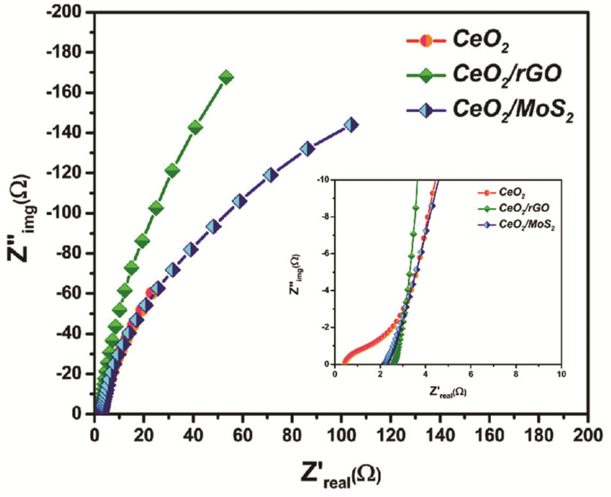

Fig. 7 — Electrochemical impedance spectra of CeO_2, CeO_2/ rGO, and CeO_2/MoS_2 nanocomposite.

both composites compared to the pure CeO_2, which shows the low charge transfer resistant (R_{ct}) of composites. The R_{ct} is responsible for the contact resistance between current collector and electrode material. Hence, the high conductive rGO and MoS_2 in the composite electrode reduce the R_{ct} which increase the conductivity of the electrode material[25].

The straight line of the Nyquist plot at lower frequency is related to Warburg frequency dependence of ion diffusion in the electrolyte. The CeO_2/rGO shows vertical line close with larger slope, which confirms the diffusive dominant ionic transport in the sample. The slope of the linear region of CeO_2 and CeO_2/MoS_2 was relatively smaller at lower frequency shows higher resistance. The large Warburg region of these electrodes show greater variation in ion diffusion path lengths and increased obstruction of ion movement. The vertical linear region with large slope indicate fast diffusion of ion in the electrolyte during charging and discharging process. The presence of rGO with high electrical conductivity resulted in a lower resistance of charge transfer in CeO_2/rGO composite electrode and hence it shows high specific capacitance compared to other electrodes .[32-37]

Conclusion

The pure CeO_2, CeO_2/rGO, and CeO_2/MoS_2 nanocomposites were successfully synthesized. The structural, morphological and electrochemical properties of the composites were comparatively investigated by XRD, SEM, FTIR, Raman Spectroscopy and electrochemical analyses. XRD pattern confirms the crystal structure of the prepared material as cubic structure and the high intense peaks illustrate the crystalline quality of the material. SEM images show the spherical morphology of CeO_2 nanoparticles on the surface of rGO and MoS_2 nanosheets. The electrochemical performance of prepared nanocomposite electrode materials was investigated by three electrodes system. CeO_2/rGO nanocomposites show high specific capacitance of 959 Fg^{-1} at 5 mVs^{-1} compared to CeO_2/MoS_2 (866 Fg^{-1}) and CeO_2 (660 Fg^{-1}). The high electrochemical performance of CeO_2/rGO nanocomposites is mainly due to anchoring of CeO_2 nanoparticles on the surface of rGO, which resulted the effect of synergistic enhancement. The experimental results demonstrated that the CeO_2/rGO nanocomposite material is a promising electrode material for supercapacitor application.

Acknowledgement

This work was financially supported by RUSA 2.0 Government of India (PO-12 Anna University). The work was partially supported by Erasmus cooperative program.

References

1 Gielen D, Boshell D, Saygin M D, Bazilian N & Gorini Wagner R, *Energy Strateg Rev*, 24 (2019) 38.
2 Chen Haisheng, Thang N C, Wei Y, Chunqing T, Yongliang L & Yulong Ding, *Prog Nat Sci*, 19 (2009) 291.

3 Augustyn V, Patrice S & Bruce Dunn, *Energy Environ Sci*, 7 (2014) 1597.

4 Wang G, Lei Z & Jiujun Z, *Chem Soc Rev*, 41 (2012) 797.

5 Zhang J & Zhao X S, *Chem Sus Chem*, 5 (2012) 818.

6 Okhay O & Alexander T, *Nanomaterials*, 5 (2021) 1240.

7 Murugan E, Rubavathy J P, Janaki Raman K, Kalpana K, Akshata C R, Santhosh Kumar S & Govindaraju S, *J Nanosci Nanotechnol*, 19 (2019) 7596.

8 Murugan E, Govindaraju S & Santhoshkumar S, *Electrochim Acta*, 392 (2021) 138973.

9 González A, Eider G, Jon A B & Roman M, *Renew Sust Energy Rev*, 58 (2016) 1189.

10 Das H T, Swapnamoy D, Nigamananda D, Payaswini D, Aniruddha M & Muhammad I, *J Energy Storage*, 50 (2022) 104643.

11 Seal S, Aadithya J, Craig J N, Udit K, Tamil S S & Dean C S, *Nanoscale*, 12 (2020) 6879.

12 Singh K R B, Vanya N, Tanushri S & Ravindra P S, *RSC Adv*, 10 (2020) 27194.

13 Wexler P, Anderson B D, Gad S C, Hakkinen P B, Kamrin M & De P, *Encycl Toxicol,* (Academic Press) 1 (2005).

14 Murugan E, Santhosh Kumar S & Raman A, *Adv Mater Proc*, 3 (2018) 112.

15 Dezfuli A S, Mohammad Reza G, Hamid Reza N & Parviz N, *RSC Adv*, 5 (2015) 46050.

16 Ji Z, Xiaoping S, Minzhi L, Hu Z, Guoxing Z & Kangmin C, *Nanotechnology*, 24 (2013) 115603.

17 Kalubarme R S, Yong-Han K & Chan-Jin P, *Nanotechnology*, 24 (2013) 365401.

18 Wei C, Kangfei L, Jing T, Xiaoting K, Haiyan H, Cheng C & Daojun Z, *Chem An Asian J*, 13 (2018) 111.

19 Padmanathan N & Selladurai S, *RSC Adv*, 4 (2014) 6527.

20 Heydari H & Mohammad B G, *Appl Physics A*, 123 (2017) 1.

21 Selvakumar D P, Nagaraju M A & Jayavel R, *Emerg Mater*, 4 (2021) 1143.

22 Muthulakshmi G, Mohamed Ismail M, Arivanandhan M & Bhaskaran A, *J Mater Sci: Mater Electron*, 33 (2022) 5534.

23 Arunbalaji S, Mohamed Ismail M, Arivanandhan M, Ali A, Abdulaziz A & Jayavel R, *Bull Chem Soc Japan*, 93 (2020) 1564.

24 Thangappan R, Kalaiselvam S, Elayaperumal A, Jayavel R, Arivanandhan M, Karthikeyan R & Hayakawa Y, *Dalt Trans*, 45 (2016) 2637.

25 Arunbalaji S, Vasudevan R, Arivanandhan M, Alsalme A, Alghamdi A & R Jayavel R, *Ceram Int*, 46 (2020) 16879.

26 Muthulakshmi G, Mohamed Ismail M, Ramya R, Arivanandhan M, Arjunan S & Bhaskaran A, *Inorg Chem Commun*, (2022) 109802.

27 Murugan E, Akshata C R, Yogaraj V, Sudhandiran G & Babu D, *Ceram Int*, 48 (2022) 16000.

28 Saravanan T, Anandan P, Shanmugam M, Azhagurajan M, Mohamed Ismail M, Arivanandhan M, Hayakawa Y & Jayavel R, *Polym Bull*, 77 (2020) 3891.

29 Mohamed Ismail M, Hemaanandhan S, Mani D, Arivanandhan M, Anbalagan G & Jayavel R, *J Sol-Gel Sci Technol*, 93 (2020) 703.

30 Lin Jinliang, Guangwei W & Guoqing L, *Indian J Chem Technol*, 27 (2020) 235.

31 Yogaraj V, Gowtham G, Akshata C R, Manikandan R, Murugan E & Arumugam M, *J Drug Deliv Sci Technol*, 58 (2020) 101785.

32 Samy O, Shuwen Z, Muhammad D B & Amine E M, *Crystals*, 11 (2021) 355.

33 Chen C, Guoqing X, Shaotang D, Fei Z, Zhengwei Y, Chunyan C, Mingtan W & Rui Z, *Colloids Surf A: Physicochem Eng Asp*, 633 (2022) 127836.

34 Santhoshkumar S & Murugan E, *Appl Surf Sci*, 553 (2021) 149544

35 Ismail Mohamed M, Vigneshwaran J, Arunbalaji S, Mani D, Arivanandhan M, Sujin P J & Jayavel R, *Dalt Trans*, 49 (2020) 13717.

36 Ismail, Mohamed M, Zhong-Yun H, Arivanandhan M, Thomas Chung-Kuang Y, Guan-Ting P & Chao-Ming H, *Energies*, 14 (2021) 7114.

37 Mei B A, Jonathan L, Terri L, Sarah H T, Bruce S D & Laurent P, *J Phys Chem C*, 122 (2018) 24499.